



CHALMERS
UNIVERSITY OF TECHNOLOGY

Shear-enhanced liquid-crystal spinning of conjugated polymer fibers

Downloaded from: <https://research.chalmers.se>, 2025-11-13 09:19 UTC

Citation for the original published paper (version of record):

Jiang, H., Yang, C., Tu, D. et al (2025). Shear-enhanced liquid-crystal spinning of conjugated polymer fibers. National Science Review, 12(10). <http://dx.doi.org/10.1093/nsr/nwaf331>

N.B. When citing this work, cite the original published paper.

MATERIALS SCIENCE

Shear-enhanced liquid-crystal spinning of conjugated polymer fibers

Hao Jiang^{1,†}, Chi-Yuan Yang^{2,†}, Deyu Tu², Yueheng Zhong¹, Zhu Chen³, Wei Huang⁴, Liang-Wen Feng³, Hengda Sun¹, Christian Müller⁵, Antonio Facchetti⁶, Hongzhi Wang^{1,*}, Simone Fabiano^{1,2,*} and Gang Wang^{1,7,*}

¹State Key Laboratory of Advanced Fiber Materials, College of Materials Science and Engineering, Donghua University, Shanghai 201620, China;

²Laboratory of Organic Electronics, Department of Science and Technology, Linköping University, Norrköping SE-60174, Sweden;

³Key Laboratory of Green Chemistry & Technology, Ministry of Education, College of Chemistry, Sichuan University, Chengdu 610065, China;

⁴School of Automation Engineering, University of Electronic Science and Technology of China, Chengdu 611731, China;

⁵Department of Chemistry and Chemical Engineering, Chalmers University of Technology, Göteborg 41296, Sweden;

⁶School of Materials Science and

Engineering, Georgia Institute of Technology, Atlanta, GA 30332, USA and ⁷Yuyue Home Textile Co., Ltd, Binzhou 256623, China

*Corresponding

authors. E-mails:

wanghz@dhu.edu.cn;

simone.fabiano@liu.se;

gwf8707@dhu.edu.cn

[†]Equally contributed to this work.

Received 23 March

2025; Revised 19 July

2025; Accepted 11

August 2025

ABSTRACT

Conjugated polymer fibers hold great promise for manufacturing unconventional electronic devices, particularly for advancing the applicability of wearable technology and smart textiles. For instance, these fibers have recently been used for energy conversion, electrochemical sensing and platforms for human–machine interactions. However, the limited methods available for spinning fibers from conjugated polymers with rigid backbones have impeded progress in wearable applications. Here, we report the continuous production of anisotropic semiconductor fibers by modulating π – π stacking interactions of liquid-crystalline conjugated polymers under shear stress. This method allows rigid conjugated polymers to be processed, synergistically enhancing both the mechanical and semiconductor properties of fibers through liquid-crystal spinning. As a result, these fibers exhibit excellent electrochemical performance, high mechanical strength (~ 600 MPa) and outstanding scalability, as well as stability under extreme temperatures, UV radiation and chemical reagent exposure. Moreover, a fully textile-based visual logic sensing system was developed using semiconductor-fiber organic electrochemical transistors, offering a novel technological approach for integrating smart textiles into precision medicine and health monitoring. These findings underscore the importance of the liquid crystalline state and solution control in optimizing the performance of conjugated polymer fibers, paving the way for developing a new generation of fiber semiconductor devices.

Keywords: liquid crystal, semiconductor fiber, fabric electronics, conjugated polymer

INTRODUCTION

π -Conjugated polymers exhibit semiconducting behavior, making them suitable for a wide range of applications such as flexible electronics, organic photovoltaics and biosensors [1–4]. Recent developments in the design and synthesis of conjugated polymers have imparted diverse electronic functionalities to fibers and textiles, enhancing their appeal for human–machine interfaces, personalized health-care and energy conversion [5–8]. Fiber-based electronic devices that can generate, transmit and modulate electronic functionalities are among the most promising forms of wearable electronics available today [9–12].

The processes used for the preparation of fabrics, such as weaving and knitting, often require fibers

and yarns to possess sufficient strength. Fibers used for mechanized garment production should possess adequate mechanical properties, such as a yield strain (ε_y) of at least several percent [13], a high yield strength (σ_y) and ideally, a high tensile strength (σ_s) comparable to common materials such as cotton ($\sigma_s > 400$ MPa) and polyester fiber ($\sigma_s > 450$ MPa). However, it remains challenging to obtain that degree of yield and tensile strength for fibers made from conjugated polymers while preserving excellent semiconductor behavior. The inherent backbone rigidity and high melting temperatures near thermal decomposition complicate the preparation of conjugated polymer fibers through methods like electrospinning and direct melt spinning [14–17].

In the case of wet spinning, poly(3,4-ethylenedioxythiophene):poly(styrenesulfonate) (PEDOT:PSS) and poly(benzodifurandione) (PBFDO) filaments with enhanced mechanical and electrochemical properties have been achieved through post-spinning drawing and coagulation bath treatments [18–21]. For example, PEDOT:PSS filaments with a σ_s of up to 410 MPa and ε_y of 2.5% have been demonstrated [20], while PBFDO filaments display a lower σ_s of up to 250 MPa and a low ε_y of only 1% [21]. However, during the spinning process, controlling the molecular state in the solution is equally crucial for enhancing the mechanical and functional properties of the fibers—a research area that is still underexplored in the context of conjugated polymer fibers [22].

Wet spinning of liquid-crystalline (LC) polymers is a widely used technique for producing high-performance fibers, including polyaramid materials such as Kevlar[®]. This technique leverages the ordered phases of LC polymers to enhance fiber properties [23,24]. Similarly, due to the planar and rigid nature of some conjugated polymers, these materials exhibit liquid-crystal phenomena enhanced by $\pi-\pi$ interactions [25]. The ordered aggregate structure formed in solution is preserved during the liquid-to-solid transition and thus persists in the solid-state fiber [26]. Applying fluid shear stress to the liquid-crystal aggregates can further enhance the $\pi-\pi$ stacking of macromolecular backbones in fibers, reducing internal flaws and facilitating high orientation and crystallinity [27]. This potentially improves the charge transport and mechanical properties of conjugated polymer fibers. However, the transition of lyotropic liquid-crystal polymers from isotropic dispersions to liquid-crystal dispersions is driven by changes in concentration [28]. Despite the potential benefits of LC spinning for conjugated polymers, their commonly lower solubility makes it difficult to create LC solutions, posing a challenge in developing suitable LC spinning processes for these materials [29].

Herein, we employed fluid shear stress to achieve continuous liquid-crystal spinning of several typical conjugated polymers by promoting $\pi-\pi$ stacking interactions, resulting in semiconductor fibers with high orientation and crystallinity. Using a combination of X-ray diffraction and electrochemical analysis, we elucidate the influence of shear stress on $\pi-\pi$ interactions, crystallinity and charge transport characteristics of these fibers. Our findings reveal that the shear-enhanced orientation of liquid-crystal molecules leads to significant uniaxial orientation in the conjugated semiconductor fibers. This results in anisotropic electrochemical properties, with axial carrier mobility and transconductance

enhanced by $\sim 400\%$ compared to the radial direction. The conjugated semiconductor fibers exhibit exceptional electrochemical properties, and also possess promisingly high yield strain and strength ($\varepsilon_y = 3.4\%$ and $\sigma_y = 383$ MPa), tensile strength ($\sigma_s \sim 600$ MPa) for textile manufacturing, and stability under extreme temperatures (-196°C to 500°C), UV radiation, and acidic or basic conditions. These attributes indicate their potential to create practical and highly adaptable logic fabrics. Furthermore, we demonstrated a large-scale, fabric-based organic electrochemical transistor (OECT) array that seamlessly integrates into textile workflows, offering real-time, non-invasive sensing (e.g. for chronic health monitoring) and paving the way toward robust, wearable smart textiles.

RESULTS AND DISCUSSION

Continuous liquid-crystal spinning of semiconductor fibers

Poly(benzimidazobenzophenanthroline) (BBL) is an example of a conjugated polymer with a rigid backbone structure. In this study, the spinning solution is pressure-driven through a microfluidic channel, where shear forces enhance the molecular orientation and thereby promote the formation of a liquid-crystal phase. The formation of this phase aligns with previous studies describing the thermotropic [30–33] or lyotropic phases [34,35] upon shearing of polymer solutions. Owing to its rigid molecular chains, which facilitate the formation of a lyotropic liquid-crystal phase [36], and its rapid proton exchange process, BBL can be continuously spun into fibers, exhibiting a high degree of uniaxial alignment (Fig. 1a, Movie S1).

We first studied the rheological behavior of BBL during the spinning process, focusing particularly on the isotropic–anisotropic phase equilibrium and shear-induced liquid-crystal formation. To this end, finite element simulations were carried out to investigate the fluid behavior of BBL₉₉ ($M_v = 33.0$ kDa; 99 repeating units) in methanesulfonic acid [BBL₉₉–methanesulfonic acid (MSA)] at various concentrations and flow velocities in the spinneret region. The results indicate that increasing the flow rate and concentration of BBL₉₉–MSA solutions increases the shear forces within the flow field (Fig. 1b, Figs S1–S4, Table S1). Calculating the fluid parameters revealed a Reynolds number (Re) ranging from 0.22 to 8.80 (Table S2), confirming that the flow remains laminar (Re < 2000). Using a 5 mg mL^{-1} BBL₉₉–MSA solution (dynamic viscosity = 4.737×10^{-2} Pa s) as an example, increasing the flow rate substantially enhances the shear forces within the fluidic field.

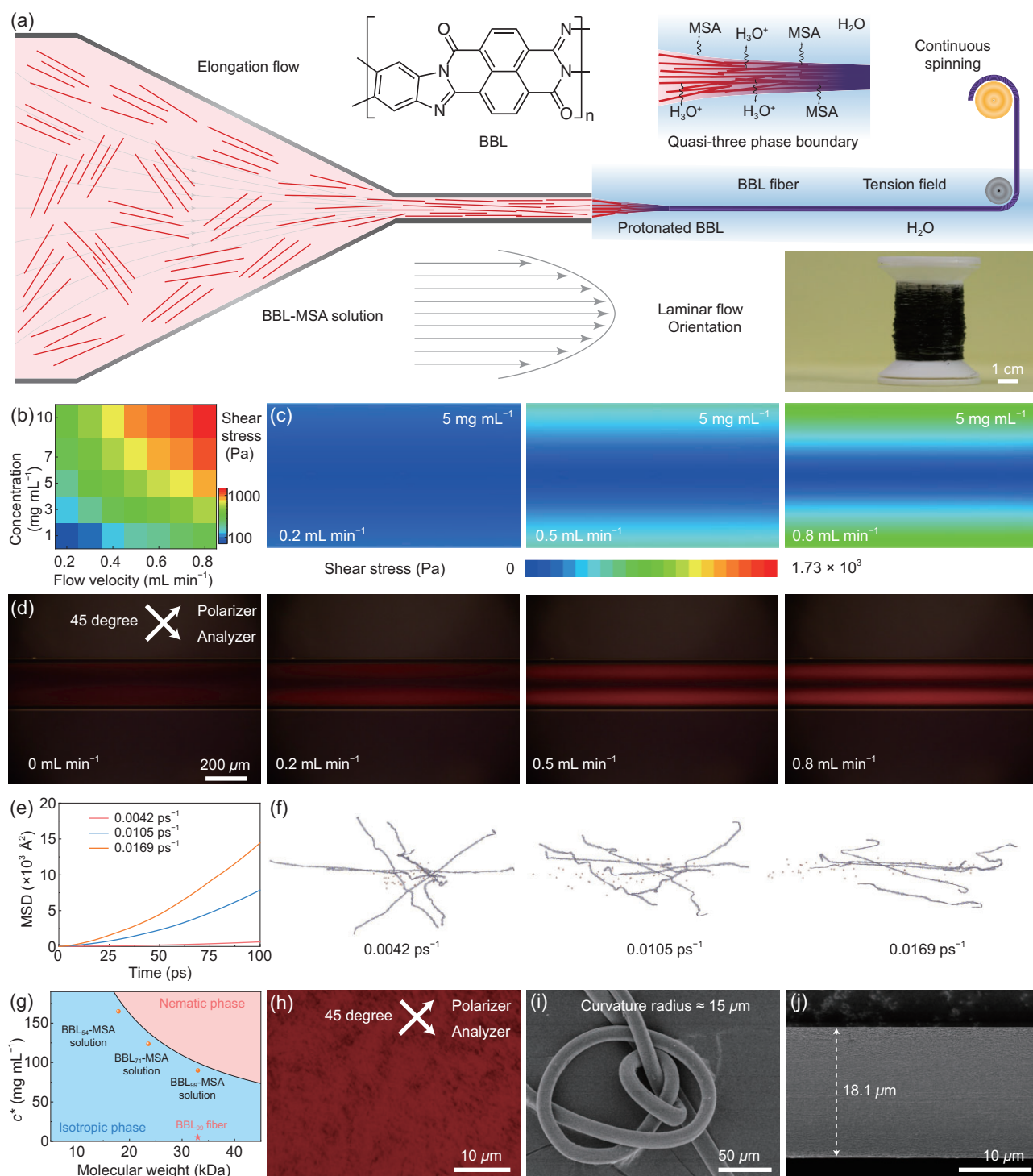


Figure 1. Continuous liquid-crystal spinning of semiconductor fibers. (a) Schematic of the fabrication process and photograph of macroscopic BBL₉₉ semiconductor fibers. (b) Thermogram showing maximum shear rates at different flow velocities and concentrations. (c) Finite element fluid simulation of shear stress distribution in a microfluidic channel (needle diameter: 200 μm) at flow rates of 0.2, 0.5 and 0.8 mL min⁻¹. (d) POM images of BBL₉₉-MSA solutions in a 200 μm-diameter glass capillary under pressure-driven nematic flow, recorded at 45° to the polarizer and analyzer. Flow rates: 0, 0.2, 0.5 and 0.8 mL min⁻¹. (e) The mean squared displacement (MSD) of N atoms in the BBL chain under thermal motion. (f) Molecular trajectory of the BBL-MSA solutions under different shear conditions. (g) Phase diagram showing the relationship between critical concentration and molecular weight in BBL-MSA solutions at 25°C. The solid black line indicates the theoretical phase boundary fitted using the Flory rigid-rod model. Blue and pink regions correspond to the isotropic and nematic liquid-crystal phases, respectively. (h) The POM image of the 90 mg mL⁻¹ BBL₉₉-MSA solution taken at 45° to the analyzer. (i) Scanning electron microscopy (SEM) image of bent BBL₉₉ fiber. (j) SEM image of BBL₉₉ fiber-0.8.

The shear force distribution obtained through finite element simulations closely corresponds to the intensity and distribution of transmitted light observed via *in situ* polarized optical microscopy (POM) at varying flow rates (Fig. 1c and d, Fig. S5). When viewed at a 45° angle to the analyzer direction, the fluid exhibits birefringence, and the transmitted light intensity increases with the flow rate.

Subsequently, the molecular dynamics of polymer chain interactions under shear stress were investigated to elucidate how shear forces induce the formation of low-concentration liquid-crystal phases (Fig. S6). To facilitate the simulation, we selected three shear rates of 0.0042, 0.0105 and 0.0169 ps⁻¹ to investigate the effect of shear force. All simulations started from the same initial state. As the shear rate increases, the slope of the mean square displacement curve of N atoms increases correspondingly (Fig. 1e), indicating that higher shear rates promote the motion of BBL molecular chains. Additionally, a larger gyration radius of N atoms and the higher radial distribution function peaks reveal the extension and aggregation of molecular chains (Fig. S7). Molecular trajectories directly show that BBL chains align in a more orderly manner and along the shear direction (Fig. 1f). Flory's molecular theory [37,38] states that the critical concentration for liquid-crystal phase formation is determined solely by the axial ratio (x). For rigid rod-like BBL molecules, the critical concentration depends on molecular weight (Fig. 1g). The calculated critical concentrations of BBL₉₉, BBL₇₁ ($M_v = 23.6$ kDa; 71 repeating units) and BBL₅₄ ($M_v = 17.9$ kDa; 54 repeating units) were 99.7, 138.5 and 181.0 mg mL⁻¹, respectively. According to Onsager's second-virial theory for rigid rods [39], the isotropic-nematic transition occurs when the gain in orientational entropy compensates for the excluded-volume penalty, resulting in a critical volume fraction that decreases inversely with x . Under shear flow, BBL chains are stretched and exhibit enhanced π - π stacking, which increases their axial ratio. Since the critical concentration is inversely related to x , even a modest increase can significantly lower the threshold required for phase transition under shear. Consequently, repeated shear deformation [40] induced the emergence of a distinct liquid-crystal texture, even below the critical concentration threshold (Fig. 1g and h, Fig. S10). Furthermore, to investigate the generality of the shear-enhanced liquid-crystal spinning method, we also examined the behavior of other conjugated polymer solutions under shear. The polybisbenzimidazobenzophenanthroline-dione (BBB), the glycolated polythiophene p(g2T-T), PBFDO, low molecular weight BBL₃₉

($M_v = 13$ kDa; 39 repeating units) and PEDOT:PSS were selected as representative conjugated polymers with flexible chains [BBB and p(g2T-T)], rigid chains (PBFDO and BBL₃₉) and mixed conjugated:non-conjugated polymer systems (PEDOT:PSS) (see Figs S11–S15 for chemical structures). Polybisbenzimidazobenzophenanthroline-dione-MSA, BBL₃₉-MSA, PBFDO-DMSO and PEDOT:PSS-H₂O were adjusted to match the dynamic viscosity of the BBL₉₉-MSA solution (5 mg mL⁻¹) by modifying their concentrations. We also increased the dynamic viscosity of p(g2T-T)-MSA as much as possible. This adjustment allowed us to characterize these conjugated polymer solutions under the same shear conditions (Table S3). In contrast to the rigid, rod-like molecular chain structure of BBL, BBB is a flexible-chain polymer that does not form LC mesophases in solution [36]. As a result, no birefringence was observed in the BBB-MSA solution (Fig. S11). However, with increasing shear force, the intensity of transmitted light and the anisotropy of birefringence increased for the BBL₃₉-MSA and PBFDO-DMSO solutions (Figs S12 and S13). In contrast, only slight birefringence was observed in the case of PEDOT:PSS-H₂O (Fig. S14), likely due to its blend system and the short rigid main chain of PEDOT. Even at a concentration of 25 mg mL⁻¹, p(g2T-T)-MSA did not reach the comparable viscosity, and no birefringence was observed (Fig. S15).

These results indicate that the pronounced birefringence observed under shear arises from the formation of a liquid-crystal phase by rigid rod-like conjugated polymers. Liquid-crystal conjugated polymer BBL₉₉ forms fibers with a well-defined annular structure, capable of bending to a radius of curvature of approximately 15 μ m (Fig. 1i). The resulting microfibers have diameters ranging from 16.10 \pm 0.09 to 18.08 \pm 0.11 μ m, depending on the flow rate (Fig. 1j, Fig. S16).

Microstructures of semiconducting fibers

Grazing-incidence wide-angle X-ray scattering (GI-WAXS) was used to characterize the microstructure of BBL₉₉ fibers (Fig. 2a–c, Fig. S17). All BBL₉₉ fibers exhibit a strong lamellar (100) diffraction peak at around $q_z = 0.76$ \AA^{-1} (d-spacing = 8.27 \AA) and a strong π - π stacking peak (010) at $q_{xy} = 1.87$ \AA^{-1} (d-spacing = 3.37 \AA) (Fig. 2d and e). As the shear effect increases during spinning, the π - π stacking distance ($d_{\pi-\pi}$) decreased from 3.52 \AA for BBL₉₉ fiber-0.2 to 3.37 \AA for BBL₉₉ fiber-0.8. The full width at half maximum (FWHM) of the π - π stacking peaks for BBL₉₉ fiber-0.2, -0.5 and -0.8 was 0.461, 0.309 and 0.279 \AA^{-1} , respectively (Fig. S18). The

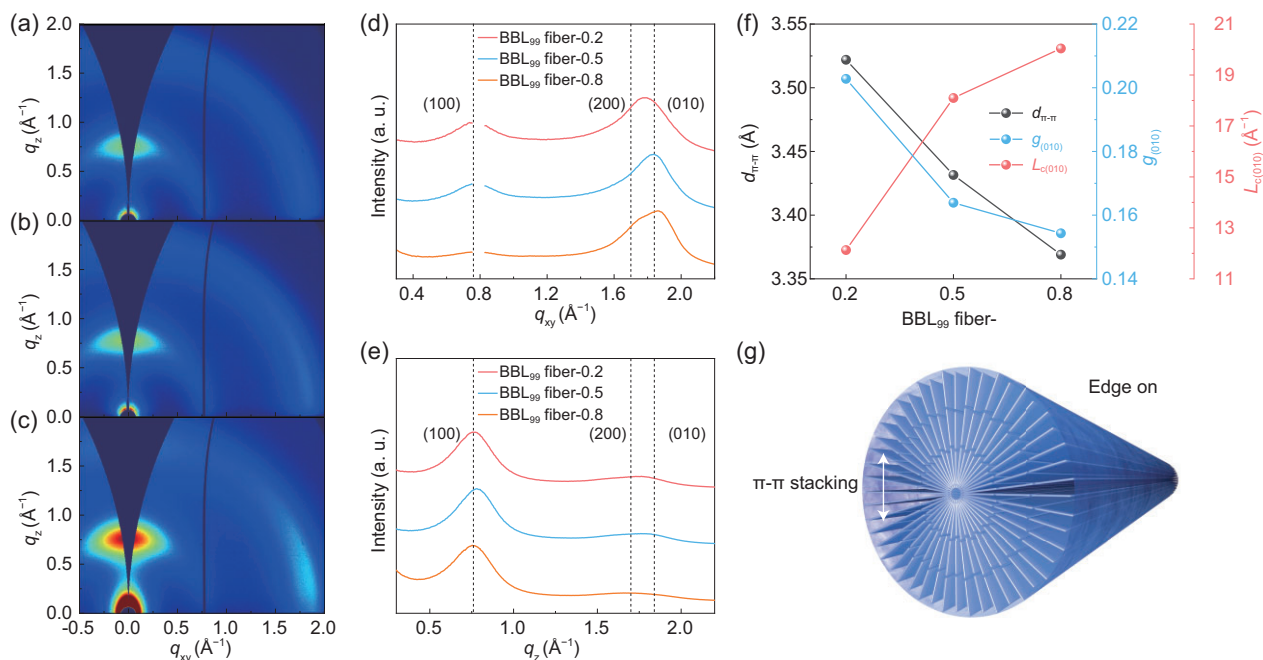


Figure 2. Microstructures of BBL fibers. (a–c) 2D GIWAXS patterns of BBL₉₉ fiber-0.2 (a), BBL₉₉ fiber-0.5 (b) and BBL₉₉ fiber-0.8 (c). (d and e) In-plane (d) and out-of-plane (e) GIWAXS line profiles of BBL₉₉ fibers. (f) $d_{\pi-\pi}$, $L_{c(010)}$ and $g_{(010)}$ of BBL₉₉ fibers. (g) Schematic of molecular packing in BBL₉₉ fibers.

slight reduction in the $\pi-\pi$ stacking distance indicates that the BBL polymer chains become more highly aligned under larger shear forces, resulting in stronger $\pi-\pi$ interactions, longer coherence length [$L_{c(010)}$] and lower paracrystalline disorder [$g_{(010)}$] (Fig. 2f, Fig. S19) [41]. This indicates that BBL molecules adopt a highly ordered edge-on orientation aligned along the fiber axis. The molecular backbone planes are aligned parallel to the fiber axis, while $\pi-\pi$ stacking occurs in the radial direction, perpendicular to the axial direction of the fibers (Fig. 2g). The results obtained for BBL₃₉ fibers also exhibit the same trend, although the changes are relatively minor owing to the shorter backbone (Figs S20–S23).

The microstructures of BBL₉₉ fiber-0.8 and films were compared using transmission wide-angle X-ray scattering (WAXS) (Fig. S24). Both BBL₉₉ fibers and films show a strong $\pi-\pi$ stacking (010) peak at around $q_z = 1.87 \text{ \AA}^{-1}$ (d-spacing = 3.37 Å), while only BBL fibers show a strong lamellar (100) diffraction peak at around $q_z = 0.76 \text{ \AA}^{-1}$ (d-spacing = 8.27 Å), which is consistent with the GIWAXS results. The WAXS diffractograms reveal that BBL fibers are oriented along the spinning direction due to extrusion through the nozzle, as indicated by the diffraction ring evolving into arcs. The WAXS curve at the (100) peak indicates that the Hermans' orientation factor [42,43] of BBL₉₉ fiber-0.8 is approximately 0.72. Compared to the

isotropy of thin films, fibers prepared with shear-enhanced liquid-crystal phases exhibit pronounced orientation.

Alignment, stability and mechanical properties of semiconducting fibers

The alignment of the BBL₉₉ fiber-0.8 was confirmed by POM (Fig. 3a, Fig. S25). To further explore the internal structure of the fibers, we used small-angle X-ray scattering (SAXS). The 1D integration of the 2D SAXS pattern yields a scattering intensity profile as a function of q (Fig. S26). A distinct diffraction arc was observed at $q_{ed} = 0.144 \text{ \AA}^{-1}$ in the equatorial direction, and it was absent in the meridian direction. This indicates the presence of a biphasic LC/isotropic structure in the BBL fiber with a periodicity of 43.8 Å [44]. Moreover, the liquid-crystal phase is aligned along the fiber axis due to the shear force.

BBL chains have planar rigid backbones that stack face-to-face, enhancing $\pi-\pi$ interactions between polymer chains [45,46]. This increased interaction correlates with a rise in tensile strength from 218 MPa (BBL₉₉ fiber-0.2) to 337 MPa (BBL₉₉ fiber-0.8) (Fig. 3b). Both σ_y and ε_y increased from 185 MPa and 1.7% to 249 MPa and 3.4%. Furthermore, BBL₃₉ and BBL₇₁ fibers with lower molecular weights exhibit a similar trend, where the tensile strength increases with enhanced shear force

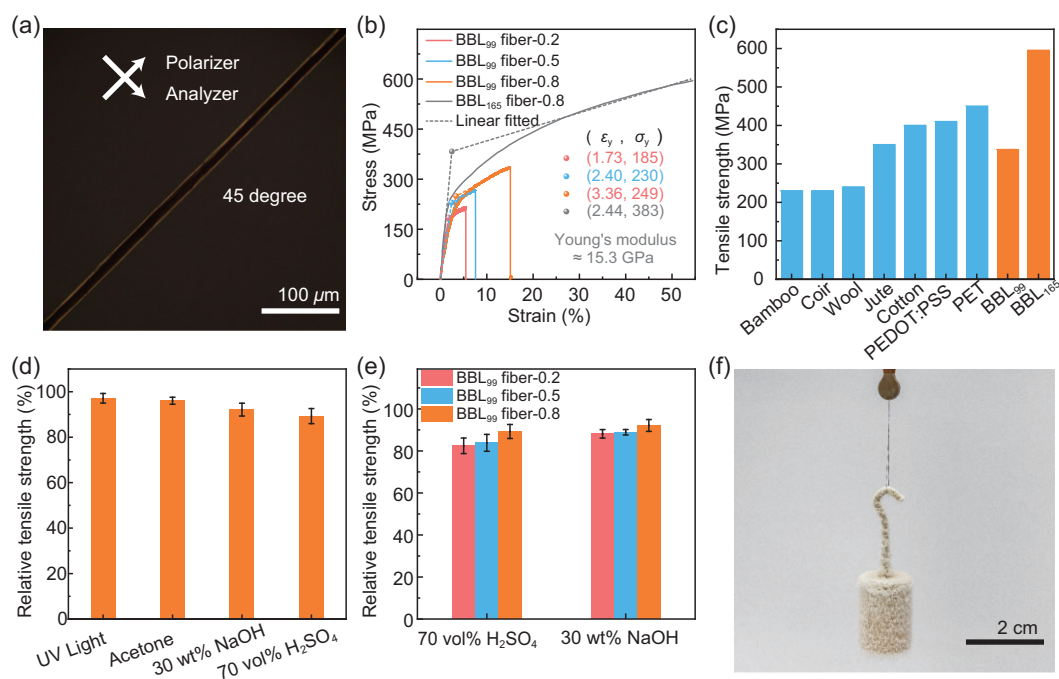


Figure 3. Alignment and mechanical performance of BBL fibers. (a) POM image of a BBL₉₉ fiber-0.8 taken with the fiber axis at 45° relative to the polarizer and analyzer. (b) Stress–strain curves of BBL₉₉ fibers and BBL₁₆₅ fiber-0.8 measured at a strain rate of 100 mm min⁻¹. (c) Tensile strength comparison between BBL₉₉ fiber-0.8 (337 MPa), BBL₁₆₅ fiber-0.8 (595 MPa) and commercial textile fibers [19, 40–42]. (d) Relative tensile strength of BBL₉₉ fiber-0.8 after UV exposure and chemical treatment. (e) Relative tensile strength of BBL₉₉ fibers after chemical reagent treatment. (f) Photograph of BBL₁₆₅ fiber carrying a 10 g weight after immersion in liquid nitrogen for 3 min. Error bars represent standard deviations from three independent measurements.

during fiber formation. In addition, the mechanical properties of the fibers are strongly dependent on the molecular weight [47]. Under the same shear condition, the tensile strengths of BBL₃₉ fiber-0.8 and BBL₇₁ fiber-0.8 are 139 ± 8 MPa and 214 ± 13 MPa, respectively (Fig. S27). Fibers spun from high-molecular-weight BBL₁₆₅ ($M_v = 55$ kDa; 165 repeating units) featured Young's modulus of 15.3 GPa, σ_s of 595 MPa and elongation at break of 54%, surpassing commonly used textile fibers [48–50] (Fig. 3b and c). The σ_y and ϵ_y values were 383 MPa and 2.4%, respectively.

The rod-like and ladder-like molecular structure imparts BBL fibers with excellent ultraviolet resistance, chemical stability and thermodynamic stability, significantly broadening their application in the field of intelligent textiles (Fig. 3d, Fig. S28). After 12-h exposure to intense UV irradiation (5000 W m⁻² at 365 nm, approximately 3500 times the conventional UV light intensity), BBL₉₉ fiber-0.8 retained 96% of its tensile strength, similarly preserved after soaking in acetone (99.5 vol%), NaOH (30 wt%) and H₂SO₄ (70 vol%) for 24 h, retaining 94%, 91% and 90% of the initial tensile strength,

respectively. Owing to their low crystallinity and orientation, BBL₉₉ fiber-0.2 and -0.5 retained only 88% and 89% of their tensile strength in NaOH solution, respectively. Similarly, they retained 82% and 85% of their strength in H₂SO₄ solution, respectively (Fig. 3e).

The high crystallinity and orientation induced by shear-enhanced liquid-crystal phases confer thermal stability to BBL fibers. Moreover, BBL₉₉ fibers are resilient to changes in temperature, as evidenced by a minimal change in tensile strain when heated from -120°C to 250°C while under constant tensile stress (Figs S29 and S30). Figure S31 shows a differential scanning calorimetry (DSC) thermogram for BBL₉₉ fiber. As previously reported [36,51], there are no observable thermal transitions between 0°C and 300°C. Thermogravimetric analysis (TGA) indicated mass retention of about 98.2% upon heating to 500°C (Fig. S32a). The fibers exhibited outstanding thermomechanical stability, remaining stable even in liquid nitrogen (Fig. 3f, Fig. S32b–d, Movie S2), which confirms their robust mechanical properties and stability in various environments.

Semiconductor fiber-based OECTs and fabric arrays

We evaluated the impact of shear-enhanced liquid-crystal phases on the functionality of BBL₉₉ fiber OECTs. The electrical and electrochemical properties of BBL fibers were extracted from OECT transfer and output measurements. The BBL₉₉ fiber was positioned across patterned Au source and drain electrodes, with the active channel covered by a 0.1 M NaCl electrolyte and biased via an Ag/AgCl gate electrode (Fig. 4a). All BBL₉₉ fiber OECTs show typical n-type accumulation-mode behavior in both output and transfer curves, as well as a standard deviation of the maximum drain current (I_{ON}) of less than 4.7% for five different devices (Fig. S33). The I_{ON}/I_{OFF} ratio increased from 2.5×10^3 for BBL₉₉ fiber-0.2 devices to 6.5×10^3 for BBL₉₉ fiber-0.8 OECTs (Fig. 4b and c, Fig. S34). At a drain voltage (V_D) and gate voltage (V_G) of 0.7 V, the drain current (I_D) reaches 0.30 ± 0.01 mA for BBL₉₉ fiber-0.2 devices compared to 0.46 ± 0.02 mA for BBL₉₉ fiber-0.8 devices. The maximum geometry-normalized transconductance ($g_{m, norm}$) increases from 2.21 ± 0.11 S cm⁻¹ for BBL₉₉ fiber-0.2 devices to 2.76 ± 0.09 S cm⁻¹ for BBL₉₉ fiber-0.8 devices (Fig. 4c, Table S4). We then calculated the product of charge-carrier mobility and volumetric capacitance (μC^*) to be 5.91 ± 0.18 , 6.59 ± 0.32 and 7.66 ± 0.48 F cm⁻¹ V⁻¹ s⁻¹ for BBL₉₉ fiber-0.2, BBL₉₉ fiber-0.5 and BBL₉₉ fiber-0.8 devices, respectively (Fig. S34, Table S5). Since C^* does not change significantly within the series, it averages 655 to 667 F cm⁻³ (Figs S35–S38), the μ ranges from $(8.98 \pm 0.65) \times 10^{-3}$ cm² V⁻¹ s⁻¹ for BBL₉₉ fiber-0.2 devices to $(1.15 \pm 0.08) \times 10^{-2}$ cm² V⁻¹ s⁻¹ for BBL₉₉ fiber-0.8 devices (Fig. 4d).

The enhanced performance of BBL₉₉ fiber-based OECTs is attributed to strong π – π interactions and increased crystallinity confirmed with GIWAXS, indicating that the formation of shear-enhanced liquid-crystal phases leads to enhanced charge transport properties of the rigid BBL polymer backbone [52,53]. Figure 4e demonstrates the robustness of the electrical output of a BBL₉₉ fiber OECT at $V_D = 0.6$ V with sequential gate bias pulses ($V_G = 0$ –0.6 V) for nearly 25 h. After more than 10 000 switching cycles, the device maintained a stable I_{ON}/I_{OFF} ratio of approximately 10^3 , demonstrating the exceptional electrochemical stability of BBL fibers in aqueous electrolytes. To the best of our knowledge, this represents the highest cycling stability reported among fiber-based OECTs to date. The response time of a BBL₉₉ fiber OECT was assessed by exponential fitting, yielding ON/OFF response times of 507 and 44 ms, respectively (Fig. S39).

The electrochemical characteristics of previously reported fiber-based OECTs are summarized in Table S6. According to the WAXS data, BBL₉₉ fibers exhibit higher orientation than the freestanding BBL₉₉ films obtained by spin-coating. As charge transport in organic semiconductors strongly depends on molecular orientation, we evaluated the electrochemical response of BBL₉₉ fibers along their axial and radial directions. A BBL₉₉ fiber-0.8 was placed in the wet state with its radial direction along the channel between the source and the drain. The electrode and electrolyte setup matched the axial BBL₉₉ fiber OECTs, which comprised a fiber with its axis aligned along the channel (Fig. 4f). We then calculated μC^* , μ and maximum $g_{m, norm}$ for radial BBL fiber OECTs to be 1.76 F cm⁻¹ V⁻¹ s⁻¹, 2.64×10^{-3} cm² V⁻¹ s⁻¹ and 0.69 S cm⁻¹, respectively (Fig. S40). Benefiting from the high degree of axial alignment, the μC^* , μ and maximum $g_{m, norm}$ extracted from axial fiber OECTs are approximately four times higher compared to those of radial fiber devices (Fig. 4g and h). In axial fiber OECT devices, charge carriers are propagated along highly coherent transport pathways enabled by enhanced π – π stacking due to the strong axial alignment of polymer chains. This ordered molecular orientation facilitates nearly unobstructed carrier transport, leading to a significant enhancement in carrier mobility. In contrast, radial transport in fiber OECTs is hindered by microstructural discontinuities perpendicular to the fiber axis, such as grain misalignments and interfacial boundaries, which introduce additional interfacial scattering and significantly reduce the effective carrier mobility [54]. As a complementary experiment, BBL₉₉ fiber-NS was fabricated under near-zero shear conditions. The corresponding OECT devices exhibited higher carrier mobility [$(0.623 \pm 0.012) \times 10^{-2}$ cm² V⁻¹ s⁻¹] compared to radial BBL fiber OECTs, thereby further confirming the critical role of molecular chain alignment in promoting efficient charge transport (Fig. S41).

Leveraging the exceptional mechanical and electrochemical properties of BBL fibers, fully textile OECT arrays were fabricated by patterning electrodes onto nanofiber fabrics and arranging BBL fibers in a structured configuration (Fig. 4I, Fig. S42). The transfer characteristics of the 6×6 OECT devices in the central region were measured to assess reliability, demonstrating outstanding device uniformity, with an average g_m of 1.39 ± 0.06 mS and I_{ON}/I_{OFF} ratio of 1557 ± 73 (Fig. 4j and k). These results highlight the process reproducibility of semiconductor-fiber OECTs and their strong compatibility with current textile manufacturing workflows.

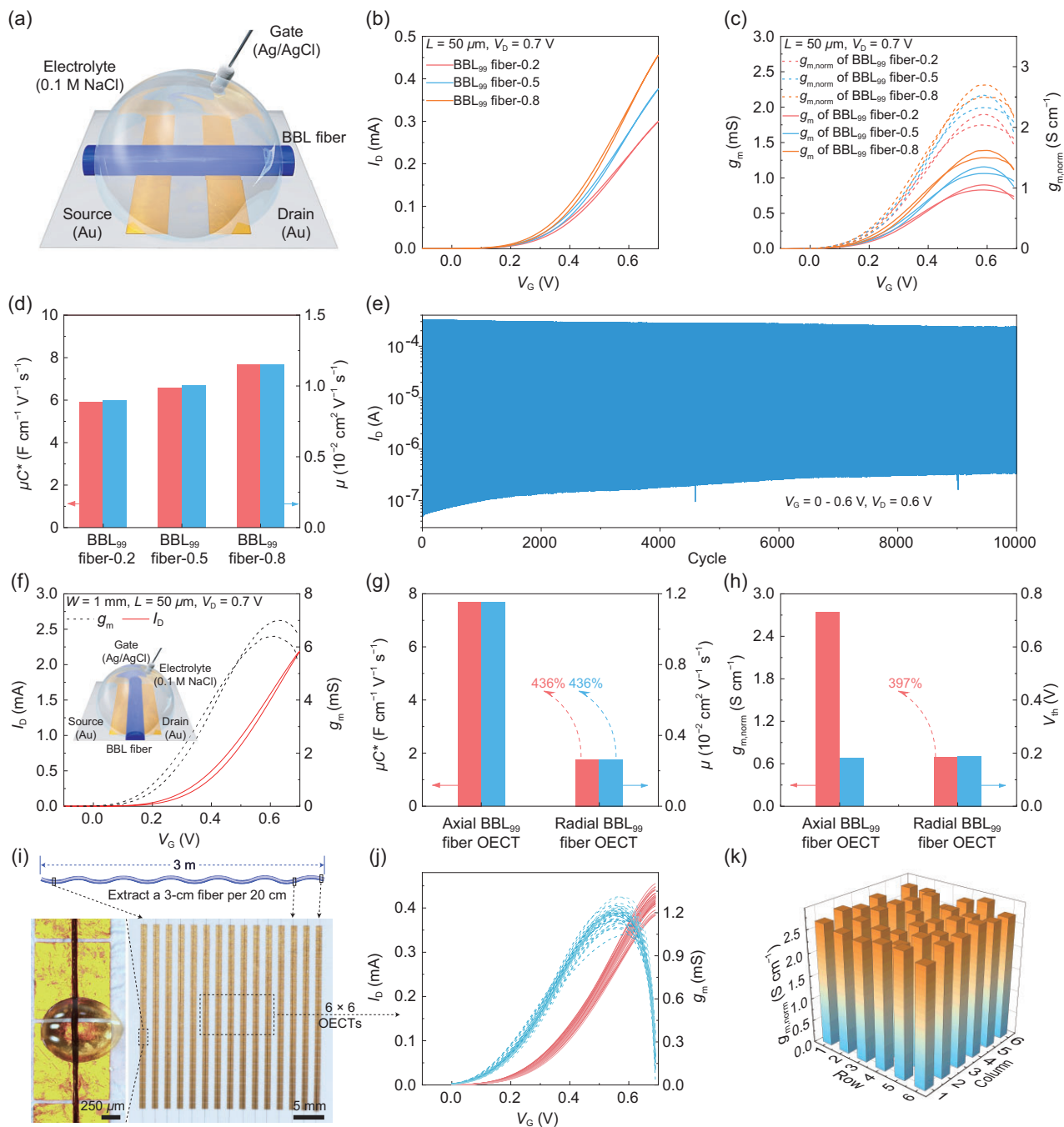


Figure 4. Semiconductor-fiber OECTs. (a) Schematic of an axially oriented BBL-fiber OECT. (b) Transfer characteristics of BBL₉₉-fiber OECTs. (c) Transconductance and $g_{m, \text{norm}}$ of BBL₉₉ fiber. (d) μC^* and μ of BBL₉₉ fiber extracted from the transfer curve. (e) Operational stability of a BBL₉₉-fiber OECT under periodic square-wave gate bias for almost 25 h. All the devices have identical geometry ($L = 50 \mu\text{m}$). (f) Schematic, transfer curve and transconductance curve of an axially oriented BBL₉₉-fiber OECT. (g) Comparison of μC^* and μ between axially and radially oriented BBL₉₉ fiber OECTs. (h) Comparison of $g_{m, \text{norm}}$ and V_{th} for axial and radial BBL₉₉-fiber OECTs. All radial devices have the same channel geometry ($L = 50 \mu\text{m}$; $W = 1 \text{ mm}$; $d = 5.06 \mu\text{m}$). (i) Photograph of a 27×15 BBL₉₉ fiber-0.8 OECT array fabricated on nanofiber fabrics. The inset shows the device structure ($L = 50 \mu\text{m}$). (j) Transfer and transconductance characteristics of 6×6 region from the fabric OECT array at $V_D = 0.7 \text{ V}$. (k) $g_{m, \text{norm}}$ across the 6×6 region of the array.

Fabric-level logic circuits

After demonstrating high-performance n-type accumulation-mode fiber OECTs, we fabricated NAND logic circuits with two, three, four and

five input signals (Fig. S43). The NAND gate is a fundamental component in digital electronics, and it can be used to build combinational logic circuits such as adders and data selectors

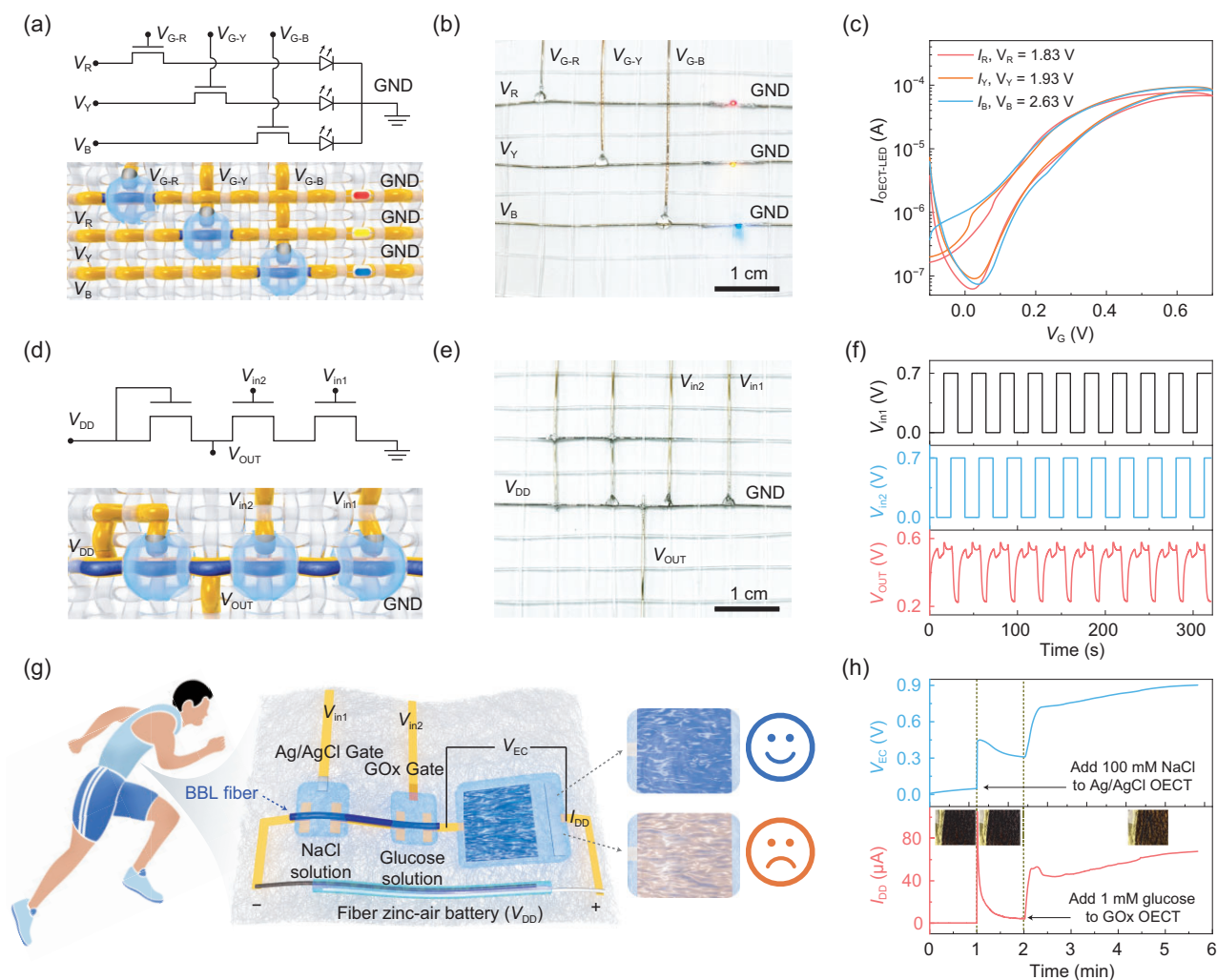


Figure 5. BBL fiber-based logic circuits. (a) Schematic and circuit diagram using fabric BBL-fiber OECTs as switches in series with RYB LEDs. (b) Photograph of the fabric-based OECT-LED circuits. (c) Output characteristics of the fabric circuit showing the positive volt-ampere response. (d) Schematic and circuit diagram of a fabric NAND gate with two input signals. (e) Photograph of the woven NAND gate circuit. (f) Output characteristics of the fabric NAND gate at $V_{DD} = 0.8$ V, where logic '0' and '1' correspond to 0.23 and 0.57 V, respectively. (g) Schematic of the fully fabric-based visualization of a logic sensing wearable system, consisting of a fiber OECT for Na^+ sensing, a fiber OECT for glucose sensing, a fabric-based electrochromic device (EC) and a fiber Zn-air battery energy storage device. (h) Visualization performance of the system in response to ionic and glucose stimuli. All devices were fabricated using BBL₉₉ fiber-0.8.

[55]. The successful implementation of these circuits highlights the potential of semiconductor fibers for building large-scale 0–1 logic gate circuits, enabling real-time portable logic operations. Poly(benzimidazobenzophenanthroline) fibers, due to their exceptional electrochemical and mechanical properties, are well suited for fabricating fabric logic circuits.

To integrate signal conversion and digital logic operations into smart textiles, we used weaving technology to construct fabric-level logic circuits with semiconductor fibers. BBL₉₉ fiber-0.8 was combined with polyimide fibers bearing patterned electrodes to form the source, drain and channel regions. Con-

ductive Ag/AgCl-coated nylon fibers served as gate electrodes. These functional fibers were woven into fabric, and solid electrolytes were applied at fabric joints to create fabric-level OECTs. The primary function of a transistor device is to serve as an electronic switch in a circuit. The fabric BBL OECT was connected in series with light-emitting diode (LED) drivers and integrated into the fabric (Fig. 5a and b). As the V_G increased, circuit current and red, yellow, blue (RYB) LED brightness increased accordingly, reaching a fully conductive state at $V_G = 0.6$ V (Fig. 5c). Fabric NAND gate logic circuits were also fabricated using BBL-fiber OECTs (Fig. 5d and e). These fabric NAND gate circuits showed

excellent performance comparable to planar devices and can communicate 0–1 digital signals (Fig. 5f). The ON-to-OFF output transitions (from digital ‘1’ to ‘0’) confirm the correct logic functionality. This capability enables the development of more complex devices and circuits, highlighting the potential for integrating intelligent circuits into textiles.

Owing to the logical versatility of NAND circuits, their application can be extended to non-invasive multi-marker sensing of biochemical indicators in human sweat. The high biocompatibility of fabric-based sensing platforms supports continuous monitoring of chronic conditions such as diabetes (Fig. 5g). In this system, the gate of a nanofiber-based OECT is functionalized with glucose oxidase (GOx) for selective glucose detection in sweat. Another OECT device with an Ag/AgCl gate responds to Na⁺ and K⁺ ions. Integration of these two OECTs forms a NAND logic-based multi-marker sensing unit. Replacing the resistive OECT in the NAND circuit with a fabric-based electrochromic (EC) device (Figs S44 and S45), integrated with fiber zinc–air batteries and functionalized OECTs, enables the creation of a fully textile-based, visually responsive wearable logic sensing system. When both OECTs are off, the driving voltage (V_{EC}) remains low, and the EC device appears dark brown. Activation of the Ag/AgCl OECT by sweat simulant exposure slightly increases V_{EC} , but it remains below the threshold for EC color change. At this stage, the EC device remains dark brown. When the GOx OECT interacts with glucose-containing sweat simulant, the enzymatic oxidation of glucose releases electrons, increases V_G and alters I_D , raising V_{EC} to approximately 0.9 V [56]. This voltage triggers a color transition in the EC device from dark brown to dark gold, visually indicating physiological state (Fig. 5h). This fully textile-integrated sensing platform meets the requirements for non-invasive, wearable and visually responsive real-time health monitoring.

CONCLUSION

In summary, we demonstrate that shear-induced formation of a lyotropic LC phase enabled the fabrication of BBL fibers with pronounced uniaxial alignment. This molecular ordering markedly enhances both mechanical and electrochemical performance, yielding anisotropic charge transport, where axial carrier mobility and transconductance were approximately four times higher compared to the radial direction. The fibers exhibit a yield strength of 383 MPa, tensile strength of 600 MPa and elongation at break of 54%, alongside excellent environmental stability. These properties make

them well suited for scalable textile manufacturing and high-performance wearable electronics. Furthermore, the development of a fully textile-integrated visual logic sensing platform integrating fiber-based sensing, energy storage and logic elements paves the way for real-time health monitoring and precision medical applications.

METHODS

The synthetic strategies and experimental parts of this work are presented in the [supplementary data](#). These methods include the fabrication of fibers, fiber OECTs, fabric circuits and the associated electrochemical and mechanical property characterization. More detailed information is provided in the [online Supplementary data](#).

SUPPLEMENTARY DATA

Supplementary data are available at [NSR](#) online.

ACKNOWLEDGEMENTS

The authors acknowledge the cooperation of the Beijing Synchrotron Radiation Facility (BSRF8.27W1A) and the Shanghai Synchrotron Radiation Facility of BL16B1 (<https://cstr.cn/31124.02.SSRF.BL16B1>) for assistance with GIWAXS measurements. The authors also acknowledge the staff of the Shanghai Synchrotron Radiation Facility (SSRF) beamline BL19U2 for help in the SAXS experiments.

FUNDING

This work was supported by the National Key R&D Program of China (2023YFC3603500 and 2024YFF0508600), the Fundamental Research Funds for the Central Universities (2232025A-06, 2232024Y-01 and CUSF-DH-T-2024003), the DHU Distinguished Young Professor Program (LZB2025002), the Key R&D Program of Shandong Province, China (2024CXGC010411), the National Natural Science Foundation of China (52373282 and 52173156), the Science and Technology Commission of Shanghai Municipality (23ZR1402000 and 24520713100) and the Taishan Industrial Experts Programme Special Funding (tscx202408117). C.M. and S.F. acknowledge funding from the Knut and Alice Wallenberg Foundation (2022.0034). This work was also supported by the Visiting Scholar Foundation of State Key Laboratory for Modification of Chemical Fibers and Polymer Materials, Donghua University.

AUTHOR CONTRIBUTIONS

H.J. and C.-Y.Y. conceived the study and contributed to the original draft preparation. G.W., H.W., H.S. and S.F. contributed to the conceptual framework. H.J., C.-Y.Y., W.H., L.-W.F. and D.T. performed methodology development. H.J., C.-Y.Y., Y.Z.,

Z.C. and G.W. conducted the investigation. G.W., H.W. and S.F. supervised the project. C.-Y.Y., L.-W.F., S.F., H.S., C.M., A.F. and G.W. contributed to writing—review and editing. All authors read and approved the final version of the manuscript.

Conflict of interest statement. None declared.

REFERENCES

- Dimov IB, Moser M, Malliaras GG *et al.* Semiconducting polymers for neural applications. *Chem Rev* 2022; **122**: 4356–96.
- Wang G, Feng L-W, Huang W *et al.* Mixed-flow design for microfluidic printing of two-component polymer semiconductor systems. *Proc Natl Acad Sci USA* 2020; **117**: 17551–7.
- Rivnay J, Inal S, Salleo A *et al.* Organic electrochemical transistors. *Nat Rev Mater* 2018; **3**: 17086.
- Ren H, Takeuchi ES, Marschilok AC *et al.* Enhancing composite electrode performance: insights into interfacial interactions. *Chem Commun* 2024; **60**: 1979–98.
- Sun F, Jiang H, Wang H *et al.* Soft fiber electronics based on semiconducting polymer. *Chem Rev* 2023; **123**: 4693–763.
- Li S, Li Y, Shao Y *et al.* Emerging two-dimensional materials constructed nanofluidic fiber: properties, preparation and applications. *Adv Fiber Mater* 2022; **4**: 129–44.
- Xing Y, Zhou M, Si Y *et al.* Integrated opposite charge grafting induced ionic-junction fiber. *Nat Commun* 2023; **14**: 2355.
- Libanori A, Chen G, Zhao X *et al.* Smart textiles for personalized healthcare. *Nat Electron* 2022; **5**: 142–56.
- Gao Z, Xiao X, Carlo AD *et al.* Advances in wearable strain sensors based on electrospun fibers. *Adv Funct Mater* 2023; **33**: 2214265.
- Zhao X, Zhou Y, Xu J *et al.* Soft fibers with magnetoelasticity for wearable electronics. *Nat Commun* 2021; **12**: 6755.
- Xu S, Xiao X, Chen J. Stretchable fiber strain sensors for wearable biomonitoring. *Natl Sci Rev* 2024; **11**: nwae173.
- Li J, Xia B, Xiao X *et al.* Stretchable thermoelectric fibers with three-dimensional interconnected porous network for low-grade body heat energy harvesting. *ACS Nano* 2023; **17**: 19232–41.
- Lund A, Wu Y, Fenech-Salerno B *et al.* Conducting materials as building blocks for electronic textiles. *MRS Bull* 2021; **46**: 491–501.
- Wang X-X, Yu G-F, Zhang J *et al.* Conductive polymer ultrafine fibers via electrospinning: preparation, physical properties and applications. *Prog Mater Sci* 2021; **115**: 100704.
- Veeramuthu L, Venkatesan M, Liang F-C *et al.* Conjugated copolymers through electrospinning synthetic strategies and their versatile applications in sensing environmental toxicants, pH, temperature, and humidity. *Polymers* 2020; **12**: 587.
- Fanous J, Schweizer M, Schawaller D *et al.* Crystalline and conductive poly(3-hexylthiophene) fibers. *Macro Mater Eng* 2012; **297**: 123–7.
- Tokito S, Smith P, Heeger AJ. Mechanical and electrical properties of poly-(2,5-thienylene vinylene) fibers. *Synth Met* 1990; **36**: 183–94.
- Kim Y, Noh H, Paulsen BD *et al.* Strain-engineering induced anisotropic crystallite orientation and maximized carrier mobility for high-performance microfiber-based organic bioelectronic devices. *Adv Mater* 2021; **33**: 2007550.
- Sarabia-Riquelme R, Andrews R, Anthony JE *et al.* Highly conductive wet-spun PEDOT:PSS fibers for applications in electronic textiles. *J Mater Chem C* 2020; **8**: 11618–30.
- Zhou J, Li EQ, Li R *et al.* Semi-metallic, strong and stretchable wet-spun conjugated polymer microfibers. *J Mater Chem C* 2015; **3**: 2528–38.
- Sarabia-Riquelme R, Noble LE, Alarcon Espejo P *et al.* Highly conductive n-type polymer fibers from the wet-spinning of n-doped PBDf and their application in thermoelectric textiles. *Adv Funct Mater* 2024; **34**: 2311379.
- Kline RJ, McGehee MD, Kadnikova EN *et al.* Dependence of regioregular poly(3-hexylthiophene) film morphology and field-effect mobility on molecular weight. *Macromolecules* 2005; **38**: 3312–9.
- Kim IH, Choi S, Lee J *et al.* Human-muscle-inspired single fibre actuator with reversible percolation. *Nat Nanotechnol* 2022; **17**: 1198–205.
- Park JH, Kim JH, Lee SE *et al.* 2D MoS₂ helical liquid crystalline fibers for multifunctional wearable sensors. *Adv Fiber Mater* 2024; **6**: 1813–24.
- Kuei B and Gomez ED. Chain conformations and phase behavior of conjugated polymers. *Soft Matter* 2017; **13**: 49–67.
- Ding L, Yu Z-D, Wang X-Y *et al.* Polymer semiconductors: synthesis, processing, and applications. *Chem Rev* 2023; **123**: 7421–97.
- Zheng W, Liu J, Guo Y *et al.* Regulation of molecular orientations of A–D–A nonfullerene acceptors for organic photovoltaics: the role of end-group π – π stacking. *Adv Funct Mater* 2022; **32**: 2108551.
- Uchida J, Soberats B, Gupta M *et al.* Advanced functional liquid crystals. *Adv Mater* 2022; **34**: 2109063.
- Liu Y, Xu Z, Gao W *et al.* Graphene and other 2D colloids: liquid crystals and macroscopic fibers. *Adv Mater* 2017; **29**: 1606794.
- Mather PT, Romo-Uribe A, Han CD *et al.* Rheo-optical evidence of a flow-induced isotropic–nematic transition in a thermotropic liquid-crystalline polymer. *Macromolecules* 1997; **30**: 7977–89.
- Mendil-Jakani H, Baroni P, Noirez L. Shear-induced isotropic to nematic transition of liquid-crystal polymers: identification of gap thickness and slipping effects. *Langmuir* 2009; **25**: 5248–52.
- Parisi D, Seo J, Nazari B *et al.* Shear-induced isotropic–nematic transition in poly(ether ether ketone) melts. *ACS Macro Lett* 2020; **9**: 950–6.
- Pujolle-Robic C and Noirez L. Observation of shear-induced nematic–isotropic transition in side-chain liquid crystal polymers. *Nature* 2001; **409**: 167–71.
- Andresen EM and Mitchell GR. Orientational behaviour of thermotropic and lyotropic liquid crystal polymer systems under shear flow. *Europhys Lett* 1998; **43**: 296.

35. Yousefi H, Wiberg G, Skytt M-L *et al.* Development and relaxation of orientation in sheared concentrated lyotropic solutions of hydroxypropylcellulose in *m*-cresol. *Polymer* 2003; **44**: 1203–10.
36. Roberts MF and Jenekhe SA. Lewis acid coordination complexes of polymers: 3. Poly(benzobisimidazobenzophenanthroline) ladder and semiladder polymers. *Polymer* 1994; **35**: 4313–25.
37. Flory PJ. Molecular theory of liquid crystals. In: Platé N.A. (ed.). *Liquid Crystal Polymers I. Advances in Polymer Science, Vol 59*. Berlin, Heidelberg: Springer, 1984.
38. Roberts MF and Jenekhe SA. Lewis acid complexation of polymers: gallium chloride complex of nylon 6. *Chem Mater* 1990; **2**: 224–6.
39. Onsager L. The effects of shape on the interaction of colloidal particles. *Ann NY Acad Sci* 1949; **51**: 627–59.
40. Kim JE, Han TH, Lee SH *et al.* Graphene oxide liquid crystals. *Angew Chem Int Ed* 2011; **50**: 3043–7.
41. Rivnay J, Noriega R, Kline RJ *et al.* Quantitative analysis of lattice disorder and crystallite size in organic semiconductor thin films. *Phys Rev B* 2011; **84**: 045203.
42. Müller C, Esmaili M, Riekel C *et al.* Micro X-ray diffraction mapping of a fluorene copolymer fibre. *Polymer* 2013; **54**: 805–11.
43. Wang X, Zhang Z, Li P *et al.* Ultrastable n-type semiconducting fiber organic electrochemical transistors for highly sensitive biosensors. *Adv Mater* 2024; **36**: 2400287.
44. Kádár R, Spirk S, Nypelö T. Cellulose nanocrystal liquid crystal phases: progress and challenges in characterization using rheology coupled to optics, scattering, and spectroscopy. *ACS Nano* 2021; **15**: 7931–45.
45. Grimme S. Do special noncovalent π – π stacking interactions really exist? *Angew Chem Int Ed* 2008; **47**: 3430–4.
46. Nayak K and Mark JE. Chain packing in two aromatic heterocyclic polymers, one of which has a ladder structure. *Makromol Chem* 1986; **187**: 1547–50.
47. Nunes RW, Martin JR, Johnson JF. Influence of molecular weight and molecular weight distribution on mechanical properties of polymers. *Polym Eng Sci* 1982; **22**: 205–28.
48. Vigneshwaran S, Sundarakannan R, John KM *et al.* Recent advancement in the natural fiber polymer composites: a comprehensive review. *J Cleaner Prod* 2020; **277**: 124109.
49. Lotfi A, Li H, Dao DV *et al.* Natural fiber–reinforced composites: a review on material, manufacturing, and machinability. *J Thermoplast Compos Mater* 2021; **34**: 238–84.
50. Ranjbar N and Zhang M. Fiber-reinforced geopolymer composites: a review. *Cem Concr Compos* 2020; **107**: 103498.
51. Tam TLD, Lin M, Handoko AD *et al.* High-performance & thermally stable n-type polymer thermoelectrics based on a benzyl viologen radical cation-doped ladder-type conjugated polymer. *J Mater Chem A* 2021; **9**: 11787–93.
52. Wu H-Y, Yang C-Y, Li Q *et al.* Influence of molecular weight on the organic electrochemical transistor performance of ladder-type conjugated polymers. *Adv Mater* 2022; **34**: 2106235.
53. Xu K, Sun H, Ruoko T-P *et al.* Ground-state electron transfer in all-polymer donor–acceptor heterojunctions. *Nat Mater* 2020; **19**: 738–44.
54. Kim JH, Halaksa R, Jo I-Y *et al.* Peculiar transient behaviors of organic electrochemical transistors governed by ion injection directionality. *Nat Commun* 2023; **14**: 7577.
55. Luo Z, Hrabec A, Dao TP *et al.* Current-driven magnetic domain-wall logic. *Nature* 2020; **579**: 214–8.
56. Wu W, Feng K, Wang Y *et al.* Selenophene substitution enabled high-performance n-type polymeric mixed ionic-electronic conductors for organic electrochemical transistors and glucose sensors. *Adv Mater* 2024; **36**: 2310503.